Research Square

Preprints are preliminary reports that have not undergone peer review.
They should not be considered conclusive, used to inform clinical practice,
or referenced by the media as validated information.

HV-Bus-Assisted Flyback Converter With Only One Additional Active Switch for Leakage- Energy Recycling and Full-Range Soft Switching

Chih-Lung Shen
National Kaohsiung University of Science and Technology
Ho-Teng Huang
I1131521140nkust.edu.tw

National Kaohsiung University of Science and Technology
You-Lin Jian
National Kaohsiung University of Science and Technology
Chung-Hsiu Shih
National Kaohsiung University of Science and Technology

Article

Keywords: Flyback converter, leakage-energy recycling, full-range soft switching, isolated DC–DC converter, low component count

Posted Date: November 4th, 2026

DOI: https://doi.org/10.21203/rs.3.rs-11239319/v1

License: This work is licensed under a Creative Commons Attribution 4.0 International License.
Read Full License

Additional Declarations: No competing interests reported.

HV-Bus-Assisted Flyback Converter With Only One Additional Active Switch for Leakage-Energy Recycling and Full-Range Soft Switching

Chih-Lung Shen[1], Ho-Teng Huang[1]*, You-Lin Jian[1], and Chung-Hsiu Shih[1]

1. Department of Electronic Engineering, National Kaohsiung University of Science and Technology, Kaohsiung, Taiwan

*Corresponding author: Ho-Teng Huang. Email: I113152114@nkust.edu.tw

Abstract

This paper proposes an HV-bus-assisted flyback converter (HBAFC) for systems with a common-ground HVDC bus and battery. The HBAFC is supplied directly from the battery and, with only one auxiliary diode connected to the existing HVDC bus, can recycle transformer leakage energy and clamp the main-switch voltage. Replacing the diode with an actively controlled switch establishes the reverse current in the leakage inductance required for ZVS turn-on of the main switch over the full operating range. Since the HBAFC does not depend on the power stage or switching operation of the existing bidirectional converter between the HVDC bus and battery, it operates independently and supports modular expansion to different output voltage and power ratings. The operating principles, steady-state characteristics, device stresses, and ZVS condition are analyzed and discussed in detail. Three 200-W HBAFC modules with 12-, 24-, and 48-V outputs have been built and experimentally tested. The results confirm independent operation, leakage-energy recycling, and main-switch ZVS turn-on. In the active-switch version, the full-load efficiencies of the 12-, 24-, and 48-V modules are 89.6%, 94.2%, and 96.1%, respectively.

***Index Terms*—Flyback converter, leakage-energy recycling, full-range soft switching, isolated DC–DC converter, low component count.**

I. Introduction

With the expanding deployment of AI data centers, electric vehicles, renewable-energy systems, and DC microgrids, battery energy storage and isolated low-voltage power supplies are increasingly required [1]–[4]. As illustrated in Fig. 1, these systems commonly comprise an HVDC bus and a battery connected through a nonisolated bidirectional DC–DC converter [5], [6]. Meanwhile, isolated low-voltage loads, such as controllers, communication equipment, and auxiliary electronics, are supplied by the battery through additional isolated DC–DC converters.

For the isolated low-voltage loads, the flyback converter is widely used for low- to medium-power supplies because it provides galvanic isolation with only one main active switch and one magnetic component, resulting in a simple, low-cost circuit structure [7]–[9]. However, the relatively large leakage inductance of the coupled inductor causes a high voltage spike across the main switch when it is turned off. A snubber is therefore commonly used to suppress the voltage spike, but the leakage energy is dissipated in the snubber, resulting in additional power loss. Moreover, the main switch still suffers from relatively high voltage stress and hard-switching conditions, thereby further increasing switching losses and electromagnetic interference. Various techniques have been proposed to recycle the leakage energy, reduce the switch-voltage stress, and achieve soft switching. Passive, lossless snubber circuits can suppress the voltage spike or redirect part of the leakage energy [10]–[13]. Active-clamp flyback converters employ an auxiliary switch and a clamp capacitor to recycle the leakage energy and achieve zero-voltage switching (ZVS) [14]–[17]. Other auxiliary resonant circuits can also provide leakage-energy recycling, voltage clamping, and soft switching

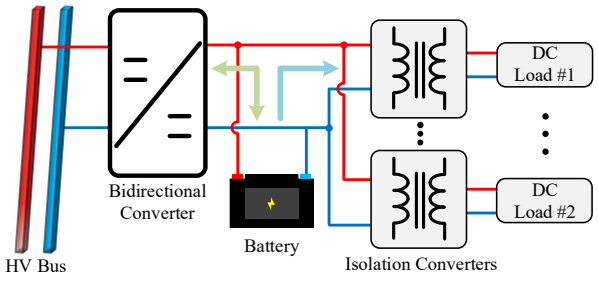


Fig. 1. Conventional HVDC bus and battery system with isolated low-voltage loads.

[18]–[20]. However, although these techniques address the aforementioned limitations, the required auxiliary components increase conduction loss and circuit complexity, thereby partially compromising the inherent advantages of the flyback converter, including its simple circuit structure and low component count.

Three-port converters have also been extensively investigated as a means of integrating the HVDC bus, battery, and isolated low-voltage load into a single power-conversion architecture [21]–[25]. Multiwinding transformers or coupled magnetic components have been employed to establish multiple power-transfer paths while reducing the number of magnetic components [21], [22]. Other approaches integrate the bidirectional and isolated conversion stages by sharing active switches, switching nodes, or a capacitor to improve component utilization and enable direct power distribution among the three ports [23], [24]. In addition, soft-switching techniques have been incorporated into three-port structures to recycle leakage energy, reduce device voltage stress, and improve switching performance [25], [26]. However, in these three-port converters, different power-transfer paths often share magnetic components, energy-storage elements, or switching states, making independent control of each path more difficult. As a result, adding multiple isolated outputs with different voltage or power specifications becomes difficult and requires redesigning the circuit parameters.

To retain the simple structure of the flyback converter while improving its switching performance, this paper proposes an HV-bus-assisted flyback converter (HBAFC) that utilizes the existing HVDC bus to provide an auxiliary path for the flyback converter, as shown in Fig. 2. In its simplest implementation, only one additional diode is required to redirect the leakage energy to the existing HVDC bus, thereby recycling the leakage energy and clamping the main-switch voltage. For applications that require soft-switching, the diode can be replaced with an active switch. The same auxiliary path can actively establish the reverse current required to discharge the main-switch output capacitance before turn-on, thereby achieving full-range ZVS while retaining the leakage-energy-recycling and voltage-clamping functions. Moreover, the operation of the HBAFC does not require integration with the bidirectional converter and can be controlled independently, allowing existing systems to be directly extended with modules of different voltage and power ratings.

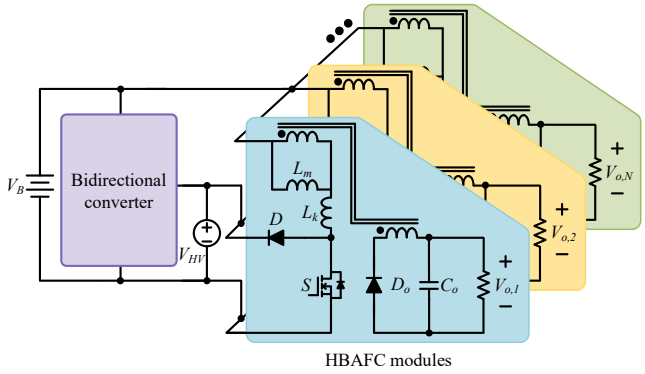


Fig. 2. Proposed HBAFC in the common ground battery and HV bus system.

II. Proposed HBAFC and Operation Principle

For a complete analysis of the proposed HBAFC, the following discussion considers the active-switch configuration of the auxiliary path. In this configuration, the diode D shown in Fig. 2 is replaced by the auxiliary switch S_2. The complete circuit configuration and the definitions of the voltage and current polarities are illustrated in Fig. 3. The transformer leakage inductance L_k is considered in the following analysis, and a conventional bidirectional buck-boost converter, consisting of L_1, S_a, and S_b, is used to clarify that the operation of the HBAFC is independent of the topology and switching states of the existing bidirectional converter. The key theoretical waveforms are shown in Fig. 4. D_1 denotes the duty ratio of the main switch S_1, which regulates the output voltage, whereas D_2 denotes the duty ratio of the auxiliary switch S_2, which is used to establish the reverse current required for ZVS. In addition, S_2 is turned on before S_1, and a dead time is inserted between their gating signals to ensure the required switching transition. Since the transformer leakage inductance L_k is considered, D_x and D_y are introduced to represent the normalized intervals associated with the rise and fall of i_{Lk}, respectively. The equivalent circuits corresponding to each operating interval in the key theoretical waveforms are shown in Fig. 5. The following analysis is conducted based on the following assumptions:

1) The output capacitor C_o is sufficiently large, and V_o is therefore assumed constant within each switching period.
2) The turns ratio of the coupled inductor is defined as $n = N_2/N_1$.
3) All semiconductor devices are assumed to be ideal, while the switch body diodes are considered.
4) The converter operates in steady-state mode, and L_m operates in continuous-conduction-mode (CCM) conditions.
5) The coupling coefficient k is defined as $L_m/(L_m+L_k)$

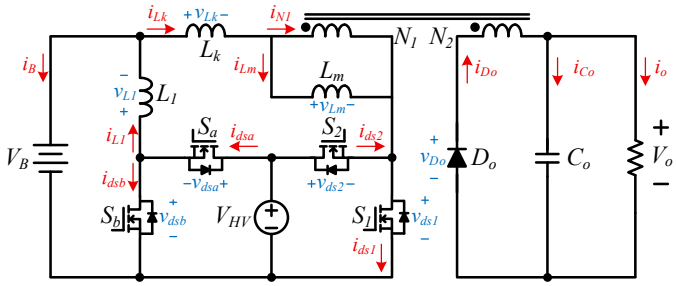


Fig. 3. Equivalent circuit of HBAFC.

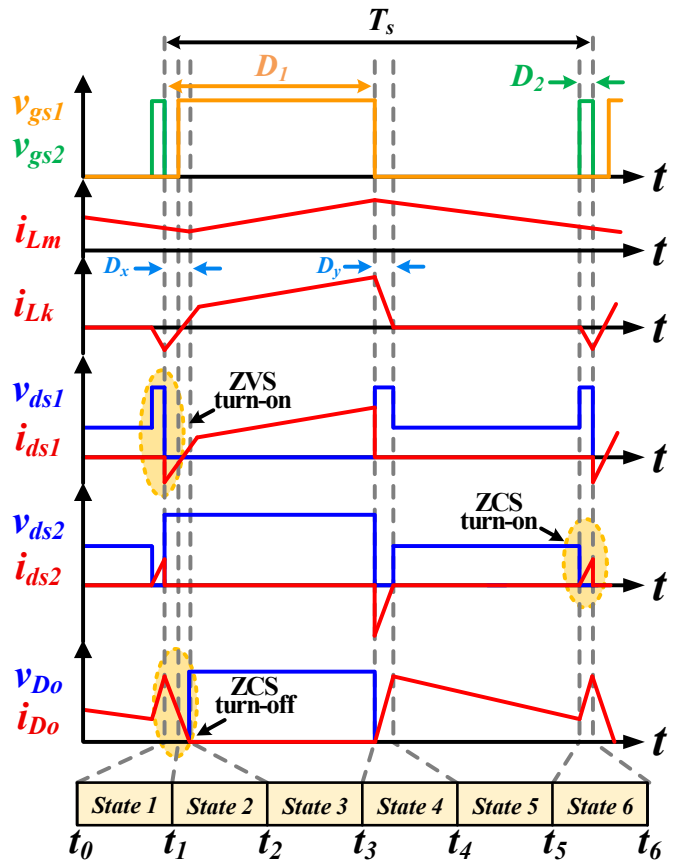


Fig. 4. Theoretical waveforms of the HBAFC.

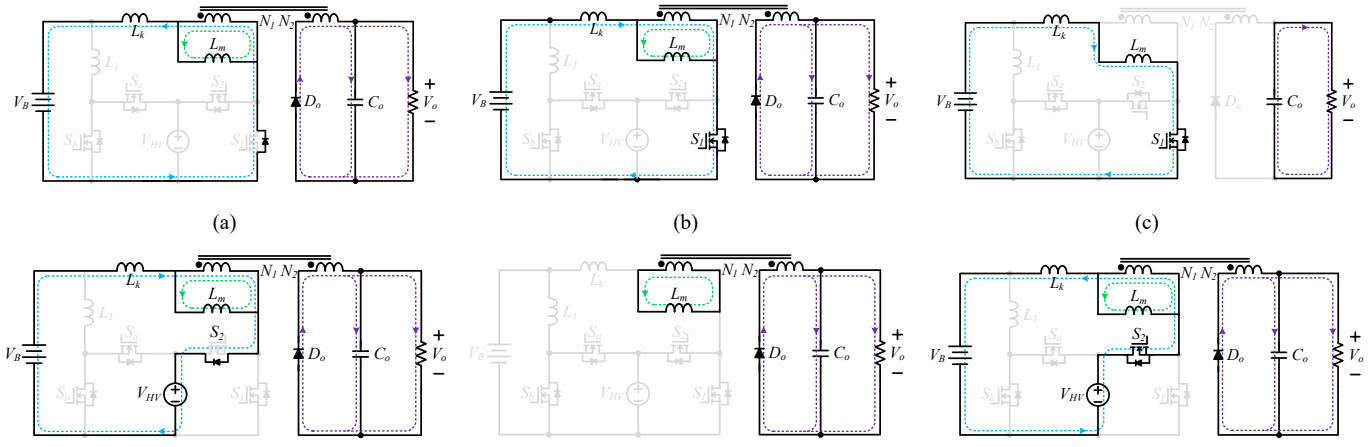


Fig. 5. Equivalent circuits of HBAFC. (a) State 1. (b) State 2. (c) State 3. (d) State 4. (e) State 5. (f) State 6.

State 1[$t_0 \sim t_1$]: This state begins when S_2 is turned off at $t = t_0$ and corresponds to the dead time interval between S_1 and S_2, as shown in Fig. 5(a). During this interval, the energy stored in L_k is released through the body diode of S_1 to V_B, while energy is transferred from N_1 to the output. Meanwhile, L_m continues to deliver energy to the output.

State 2[$t_1 \sim t_2$]: After the short dead-time interval, this state begins when v_{gs1} goes high, as shown in Fig. 5(b). Since the body diode of S_1 is already conducting, the voltage across S_1 is clamped to zero before the gate signal is applied. Therefore, S_1 is turned on under ZVS. During this state, the operating conditions remain the same as the previous state, and i_{Lk} continues to increase. According to KVL, the voltages across L_m and L_k can be expressed as:

$$v_{Lm}(t) = \frac{-V_o}{n} \tag{1}$$

$$v_{Lk}(t) = V_B + \frac{V_o}{n}. \tag{2}$$

State 3[$t_2 \sim t_3$]: This state begins when i_{Lk} increases to i_{Lm}, at which instant i_{Lm} reaches its minimum value, $i_{Lm,min}$, as shown in Fig. 5(c). The output diode D_o is turned off under zero-current switching (ZCS). In this state, V_B supplies energy to the L_k and L_m in series, and their currents increase with the same slope. The voltages across L_k and L_m can be expressed as:

$$v_{Lm}(t) = V_B k \tag{3}$$

$$v_{Lk}(t) = V_B(1-k). \tag{4}$$

State 4 [$t_3 \sim t_4$]: This state begins when S_1 is turned off, as shown in Fig. 5(d). The magnetizing inductance L_m begins to release energy to the output through the secondary winding N_2. Meanwhile, the body diode of S_2 provides a freewheeling path for i_{Lk}, allowing the energy to be recycled to V_{HV} while clamping the voltage across S_1 to V_{HV}. The voltages across L_k and L_m can be expressed as:

$$v_{Lm}(t) = \frac{-V_o}{n} \tag{5}$$

$$v_{Lk}(t) = V_B + \frac{V_o}{n} - V_{HV}. \tag{6}$$

During this interval, i_{Lk} decreases linearly from its peak value to zero. The duration D_y of this state is obtained from (6) by substituting the magnetizing current ripple expression as follows:

$$D_y = -\frac{L_k f_s \left(I_{Lm,avg} + 0.5\Delta i_{Lm}\right)}{v_{Lk}(t)}. \tag{7}$$

State 5 [$t_4 \sim t_5$]: This state begins when i_{Lk} decreases to zero, as shown in Fig. 5(e). At this instant, the body diode of S_2 is turned off under ZCS. Meanwhile, L_m continues to release its energy to the output through the secondary winding N_2 as in the previous state.

State 6 [$t_5 \sim t_6$]: This state begins when S_2 is turned on, as shown in Fig. 5(f). The magnetizing inductance L_m continues to transfer its energy to the output through N_2. In addition, V_{HV} begins to energize L_k in the reverse direction, and the voltage across L_k is:

$$v_{Lk}(t) = V_B + \frac{V_o}{n} - V_{HV}. \tag{8}$$

When S_2 is turned off, this state ends, and the converter completes one switching cycle.

III. Steady-State Analysis

A Voltage Gain

To derive the voltage gain, the volt-second balance is applied to L_m and L_k over a complete switching period, yielding the following relationships:

$$\int_{t_0}^{t_6} v_{L_m}(t)\,dt = \frac{-V_o}{n} D_x T_s + kV_B(D_1 - D_x)T_s + \frac{-V_o}{n}(1-D_1)T_s = 0 \tag{9}$$

$$\int_{t_0}^{t_6} v_{L_k}(t)\,dt = (V_B + \frac{V_o}{n})D_x T_s + V_B(1-k)(D_1 - D_x)T_s + (V_B + \frac{V_o}{n} - V_{HV})(D_y + D_2)T_s = 0 \quad (10)$$

Simplifying (9) gives the voltage gain as:

$$M(D_1) = \frac{V_o}{V_B} = \frac{nk(D_1 - D_x)}{1 - D_1 + D_x}. \quad (11)$$

Similarly, (10) yields the relationship between D_x and D_y as:

$$D_x = \frac{\left(D_2 + D_y\right)\left(nV_{HV} - nV_B - V_o\right) - nV_B\left(1-k\right)D_1}{nkV_B + V_o}. \quad (12)$$

According to (7), $I_{Lm,avg}$ in D_y can be derived by applying the charge-balance condition to the output capacitor, as follows:

$$I_{Lm,avg} = \frac{ni_o}{1 - D_1 + D_x}, \quad (13)$$

Δi_{Lm} can be derived from the inductor voltage–current relationship:

$$v_{Lm} = L\frac{di}{dt}. \quad (14)$$

From State 3, the current ripple over the entire current-rising interval can be obtained as:

$$\Delta i_{Lm} = \frac{kV_B\left(D_1 - D_x\right)}{L_m f_s}. \quad (15)$$

Substituting (13) and (15) into (7) yields

$$D_y = \frac{nL_k\left(2f_s L_m I_{Lm,avg} + kV_B D_1\right)}{2L_m\left[n\left(V_{HV} - V_B\right) - V_o\right]}. \quad (16)$$

Substituting (16) into (12) yields

$$D_x = \frac{2nL_k f_s I_{Lm,avg} + 2\beta D_2 - n(1-k)V_B D_1}{2\alpha}, \quad (17)$$

where

$$\alpha = nkV_B + V_o \quad (18)$$

$$\beta = n\left(V_{HV} - V_B\right) - V_o. \quad (19)$$

Finally, substituting (17)–(19) into (11) gives the voltage gain as:

$$M(D_1) = \frac{V_o}{V_B} = \frac{k(1-D_1)nR_o I_o\left[D_1(1+k) + 2D_2\right]}{2\left\{f_s L_m n^2(1-k)I_o + k(1-D_1)\left[(1-D_1-D_2)I_o R_o + D_2 nV_{HV}\right]\right\}}. \quad (20)$$

For i_{Lk} recycling, the voltage across L_k must remain negative during State 4. Therefore, the following conditions must be satisfied:

$$V_B + \frac{V_o}{n} - V_{HV} < 0. \quad (21)$$

Substituting (20) into (21) gives the operating constraint of D_1:

$$D_1 < \frac{V_{HV} - V_B}{V_{HV} - V_B + kV_B}. \quad (22)$$

For V_B = 120 V and V_{HV} = 400 V, the maximum D_1 obtained from (22) is approximately 0.7. Based on (20), the voltage-gain characteristics versus D_1 for different n and L_k at I_o = 8.33 A are shown in Fig. 6. For small L_k, the voltage gain is significantly affected by n. As L_k increases due to lower coupling, the maximum gain becomes similarly limited, while n = 0.5 provides a higher gain.

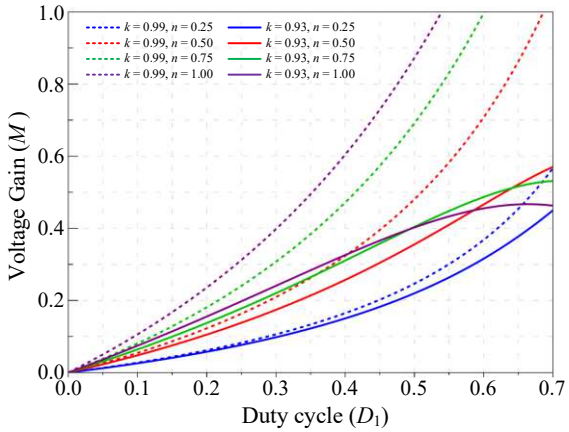


Fig. 6. Voltage-gain under different turns ratios n and leakage inductances L_k.

B. Voltage and Current Stress

Based on the operating states shown in Fig. 5, the maximum voltages across S_1, S_2, and D_o are expressed as follows:

$$V_{ds1} = V_{ds2} = V_{HV} \tag{23}$$

$$V_{Do} = nkV_B + V_o, \tag{24}$$

and the average current stresses of S_1, S_2, and D_o are given as follows:

$$I_{ds1} = I_{Lm} D_1 \tag{25}$$

$$I_{ds2} = (I_{Lm} + nI_o) D_2 \tag{26}$$

$$I_{Do} = \frac{I_{Lm}}{n}(1 - D_1). \tag{27}$$

$$I_{Lm,avg} = \frac{ni_o\left[(1 - D_1)\gamma - \delta\right]}{(1 - D_1 - D_2)\gamma + ni_o L_k f_s}, \tag{28}$$

where

$$\gamma = kV_B + \frac{V_o}{n} \tag{29}$$

$$\delta = \left(V_{HV} - V_B - \frac{V_o}{n}\right) D_2 - \frac{(1 - k)V_B D_1}{2}. \tag{30}$$

C. Magnetizing Inductance and Capacitor

Typically, the BCM operating point is set at approximately 25%–50% of the full-load output current. At the BCM boundary, the minimum magnetizing current is zero. Therefore, by applying $I_{Lm,avg}$ - 0.5Δi_{Lm} = 0 into (13) and (15), the required magnetizing inductance is obtained as

$$L_m = \frac{V_o (1 - D_1 + D_x)^2}{2n^2 i_{o,BCM} f_s}. \tag{31}$$

Fig. 7 shows the required magnetizing inductance versus duty ratio when the BCM boundary is set at 30% of the full-load output current (I_o = 2.5 A), where the transformer coupling coefficient is assumed to be 0.93. For D_1 > 0.3, the required L_m remains approximately within 90–110 μH.

As for the capacitor design, voltage ripple is the main consideration. Accordingly, applying charge balance yields the voltage ripple of C_o in the proposed converter as follows:

$$\Delta v_o = \frac{V_o D_1}{R_o C_o f_s}. \tag{32}$$

Based on (32), the voltage ripple ratios of C_o are given as follows:

$$\varepsilon_o\% = \frac{\Delta v_o}{V_o} = \frac{D_1}{R_o C_o f_s} \tag{33}$$

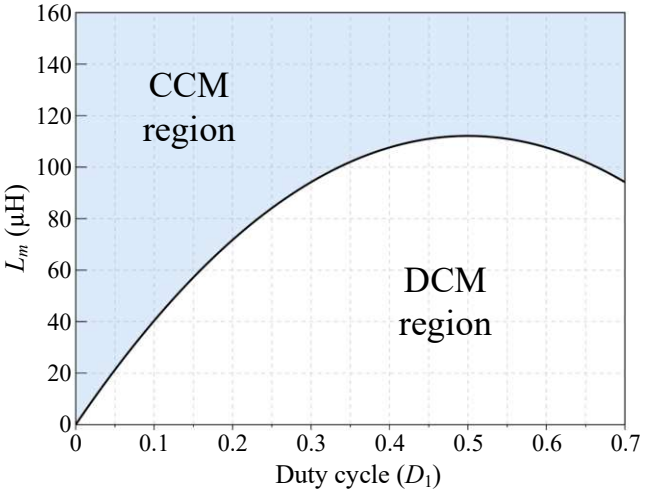


Fig. 7. Required magnetizing inductance versus duty ratio at the BCM boundary of 30% full-load output current.

D. Efficiency Analysis

Fig. 8 shows the equivalent circuit of the HBAFC for power-loss analysis. The total power loss is expressed as follows

$$P_{Total_Loss} = P_{S_Cond} + P_{S_Sw} + P_D + P_{Cap} + P_L . \tag{34}$$

where P_{S_Cond}, P_{S_Sw}, P_D, P_{Cap}, and P_L denote the switch conduction loss, switching loss, magnetic core loss, copper loss, and capacitor ESR loss, respectively. Each loss component is calculated as follows:

$$P_{S_Cond} = \sum_{j=1,2} \left(I_{dsj_rms}^2 \, r_{dsj(\text{on})} \right) \tag{35}$$

$$P_{S,Sw} = \frac{f_s}{2} \left(\sum_{j=1,2} (V_{dsj} \, I_{dsj} \, t_{fj}) + C_{oss,S2} V_{ds2}^2 \right) \tag{36}$$

$$P_D = V_{Do,f} \, I_{Do,avg} \tag{37}$$

$$P_{Cap} = I_{Co_rms}^2 \, r_{Co} \tag{38}$$

$$P_L = I_{Lm_rms}^2 r_{N1} + I_{Do_rms}^2 r_{N2} + k_{Fe} f_s^{\alpha} B_{Lm}^{\beta} V_{e_Lm} . \tag{39}$$

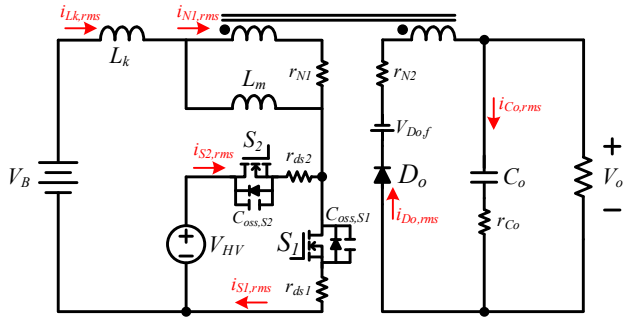


Fig. 8. Equivalent circuit of HBAFC for efficiency analysis.

The k_{Fe}, α, β, B, and V_e are the core parameters of the inductor, and f_s is the switching frequency. Fig. 9 shows the estimated efficiency under active-switching and diode-only operation of S_2. The component parameters used in the calculation are V_{HV} = 400 V, V_o = 24 V, I_o = 8.33 A, f_s = 100 kHz, n = 0.5, V_{Do_f} = 0.5 V, r_{ds1} = 50 mΩ, r_{ds2} = 80 mΩ, $C_{oss,S1}$ = 386 pF, $C_{oss,S2}$ = 100 pF, t_{S1_on} = t_{S2_on} = 30 ns, t_{S1_off} = t_{S2_off} = 20 ns, r_{N1} = 30 mΩ, r_{N2} = 15 mΩ , and r_{Co} = 15 mΩ. The results show that active switching leads to lower efficiency at light load because of the inherent reverse current required for ZVS and the switching loss of the auxiliary switch. However, as the load increases, the benefit of ZVS becomes more pronounced, leading to higher efficiency.

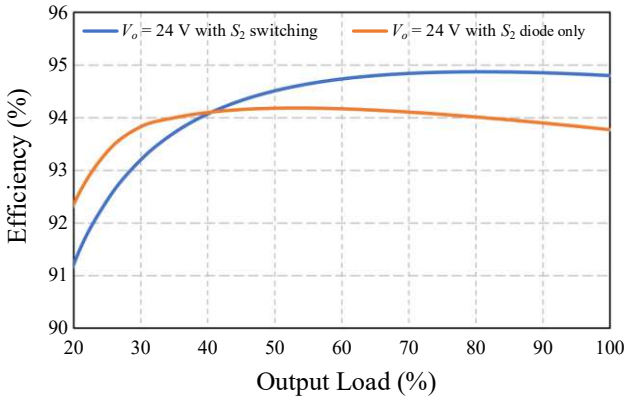


Fig.9. Estimated efficiency under active-switching and diode-only operation of S_2.

E. ZVS Condition

To achieve ZVS of S_1, $C_{oss,S1}$ must be fully discharged by the reverse current of Lk within the dead time. Therefore, the charge supplied by the reverse current during the dead time must satisfy

$$t_d \left| i_{L_k,t_0} \right| \geq C_{oss,S1} V_{HV} . \tag{40}$$

The value of $i_{Lk,t0}$ can be obtained from the t_5–t_6 interval. Rearranging (8) gives:

$$i_{Lk,t0} = \frac{(V_B - V_{HV} + V_o/n) D_2 T_s}{L_k} . \tag{41}$$

Substituting (41) into (40), the duty ratio D_2 required to complete the ZVS transition within the dead time is obtained as:

$$D_2 \geq \frac{L_k C_{oss,S1} V_{HV}}{t_d T_s \left(V_{HV} - V_B - V_o / n \right)} . \tag{42}$$

F. Control Strategies

Fig. 10 shows the digital control architecture of the HBAFC. The output-port feedback voltage $v_{o,fb}$ is compared with the reference voltage $V_{o,ref}$, and the resulting error is processed by a PID controller to determine D_1 for output-voltage regulation. A limiter is employed to constrain D_1 within the allowable operating range. In addition, D_2 is directly set according to (42) and the selected dead time. The resulting D_1 and D_2 are then applied to the PWM generator to produce the corresponding gate signals.

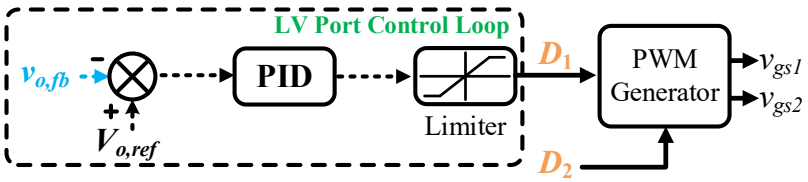


Fig.10. Control diagram of the proposed HBAFC.

IV. Performance Comparison

Table I compares the proposed HBAFC with other flyback-derived converters in terms of component count, operating specifications, auxiliary circuit, leakage-energy recycling, full-load efficiency, and main-switch soft switching. The converters in [13], [14], [19], and [20] achieve both leakage-energy recycling and main-switch soft switching, but require a higher component count, resulting in lower efficiency. Among the compared converters, [10] achieves the highest full-load efficiency of 97.6%. This high efficiency is partly due to the use of synchronous rectification rather than an output rectifier diode. However, synchronous rectification in a flyback converter requires additional current detection and switching-state determination to ensure proper rectifier-switch control, thereby increasing control complexity. In contrast, the proposed HBAFC uses the existing HVDC bus and requires only one additional auxiliary switch. This auxiliary path simultaneously enables leakage-energy recycling, main-switch voltage clamping, and the reverse current required for ZVS turn-on, while maintaining a simple power-stage and control implementation.

TABLE I
Comparison of the Proposed Converter With Other Converters

Ref.	Number of components S/D/C/M	$P/f_s/V_o$	Auxiliary circuit components	Leakage energy recycling	Full load efficiency	Main switch soft switching
[8]	1/2/2/1	50 W/50 kHz/24 V	1L, 1C	No	–	No
[10]	3/0/2/1	240 W/250 kHz/5–24 V	1L, 1C	Yes	97.6%	Yes
[13]	1/4/2/2	120 W/100 kHz/72 V	3D, 1L, 1C	Yes	93.4%	Yes
[14]	2/1/2/1	65 W/65 kHz/19 V	1S, 1C	Yes	91.6%	Yes
[19]	5/0/2/1	560 W/710 kHz/28 V	1C	Yes	92.3%	Yes
[20]	2/2/3/2	100 W/100 kHz/24 V	1S, 1D,1L, 1C	Yes	93.7%	Yes
Pro.	2/1/1/1	200 W/100 kHz/24 V	1S	Yes	94.2%	Yes

S: Switch, D: Diode, C: Capacitor, M: Magnetic core, P: Power, f_s: Switching frequency, V_o: Output voltage.

V. Experimental Results

To verify the HBAFC and demonstrate its independent operation from the bidirectional power stage between V_{HV} and V_B, a hardware prototype was constructed, as shown in Fig. 11. The HVDC-bus voltage V_{HV} was maintained at 400 V, while the battery voltage V_B was varied from 120 to 150 V. As shown in Fig. 11, the front section of the prototype contains a 400 W bidirectional converter consisting of L_1, S_a, and S_b. As shown in Fig. 12, three 200 W HBAFC modules with output voltages of 12, 24, and 48 V were connected to the same battery and HVDC bus. All three modules were operated at a fixed switching frequency of 100 kHz. The bidirectional converter and the three HBAFC modules were controlled by a single STM32G474 microcontroller. Table II lists the circuit specifications and component parameters of the bidirectional converter according to the TCM control [27], [28], and the HBAFC module with a 24 V output.

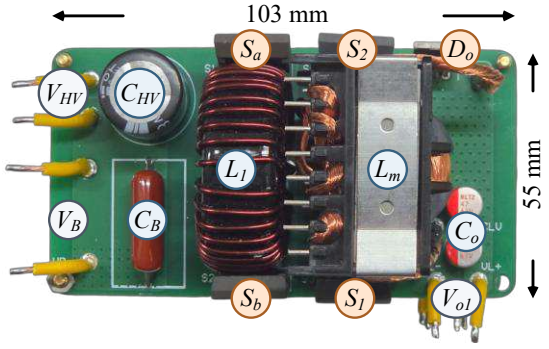


Fig. 11. Prototype front view.

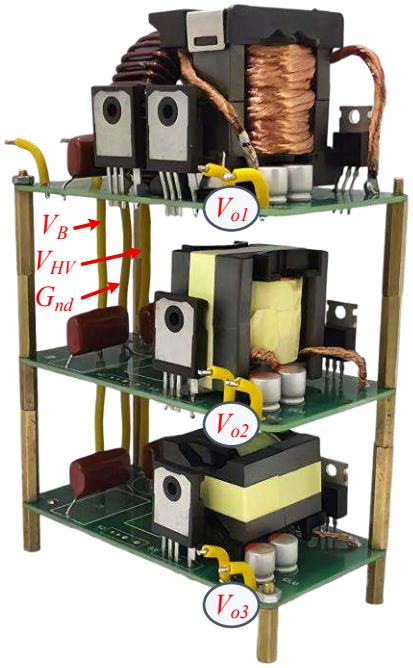


Fig. 12. Prototype side view.

Fig. 13 shows the measured full-load waveforms of the bidirectional converter. Figs. 13(a) and 13(b) show the measured waveforms of the bidirectional converter in buck mode, where S_a operates as the main switch, and S_b operates as the synchronous rectifier. Figs. 13(c) and 13(d) show the corresponding waveforms in boost mode, where S_b operates as the main switch, and S_a operates as the synchronous rectifier. These results verify bidirectional power transfer between V_{HV} and V_B under TCM control and unaffected by HBAFC operations.

TABLE II
CIRCUIT PARAMETERS OF THE EXPERIMENTAL PROTOTYPE

Parameters	Value
L_1 (Inductor)	112 μH
L_m (Inductor)	100 μH
turns ratio (N_p : N_s)	26 : 13
k (Coupling coefficient)	0.93
C_{HV} (Capacitor)	10 μF
C_B (Capacitor)	0.1 μF
C_o (Capacitor)	2×47 μF
S_a, S_b, S_1 (MOSFET)	IMZA65R010M2H
S_2 (MOSFET)	IMZA65R060M2H
D_o (Diode)	FERD20H100S

Fig. 14 shows the measured full-load waveforms of the 24 V HBAFC module with S_2 switching. Fig. 14(a) shows that i_{Lk} decreases into the negative region when S_2 is turned on. After S_2 is turned off and S_1 is turned on, the current through L_k increases until it reaches the current of L_m, then increases together, verifying the key waveforms in Fig. 4 and the steady-state analysis. Fig. 14(b) shows the ZVS turn-on of S_1, while v_{ds1} is clamped at V_{HV} = 400 V without ringing and voltage spike. Fig. 14(c) shows that the current through S_2 starts from zero and increases to approximately 8 A during its conduction interval, while the negative current represents the leakage-inductance current during leakage-energy recycling to the HVDC bus. Fig. 14(d) shows the measured voltage and current waveforms of the output diode D_o, confirming ZCS turn-off. Fig. 15 shows the measured waveforms of the 24 V HBAFC module with S_2 switching disabled. Fig. 15(a) shows that i_{Lk} does not become negative. Fig. 15(b) shows that the reverse current required for ZVS is absent, and v_{ds1} remains at approximately 120 V when S_1 is turned on. Fig. 15(c) shows that although S_2 is not actively switched, its diode still conducts i_{Lk} during leakage-energy recycling. Fig. 15(d) shows that, during the conduction interval of D_o, i_{Do} does not exhibit the current increase associated with the reverse current, and only the current of L_m continues to be transferred to the output.

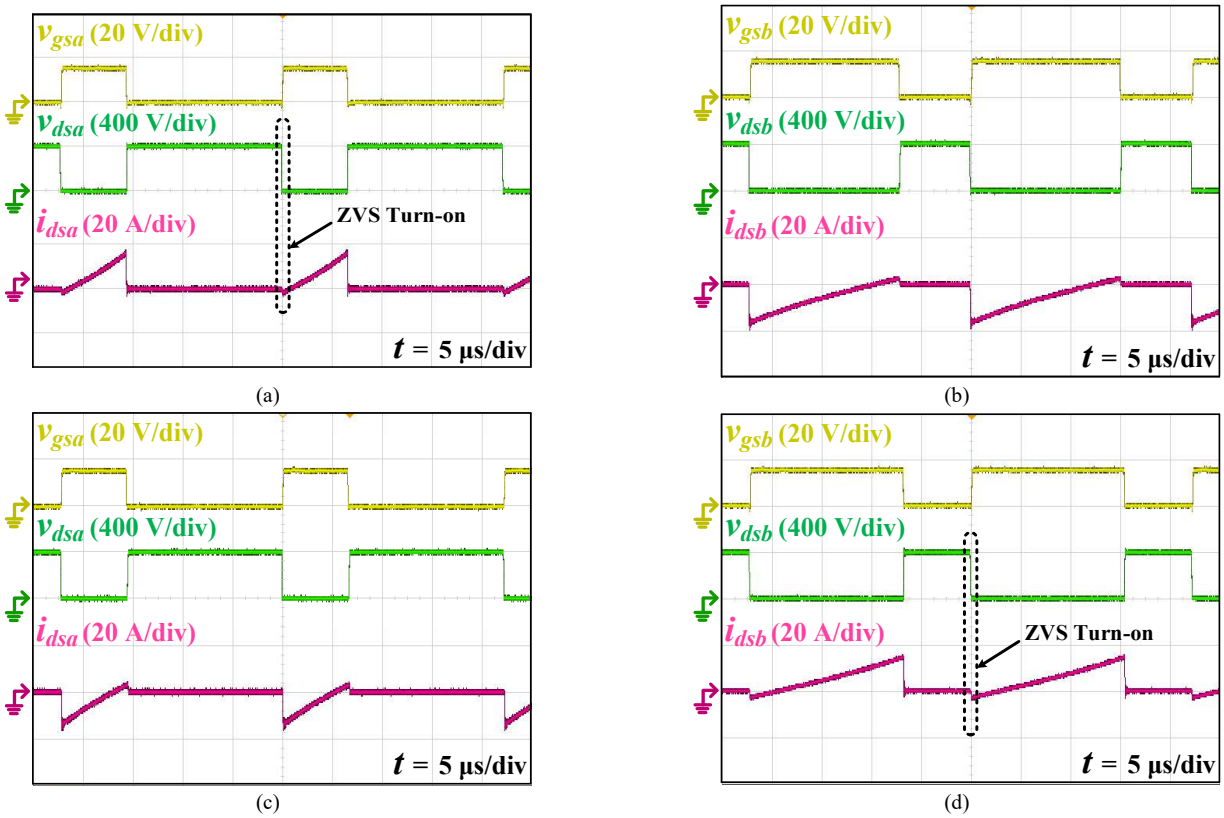


Fig. 13. Experimental waveforms of the prototype at full load. (a) Gate signal, voltage, and current of S_a in buck mode. (b) Gate signal, voltage, and current of S_b in buck mode. (c) Gate signal, voltage, and current of S_a in boost mode. (d) Gate signal, voltage, and current of S_b in boost mode.

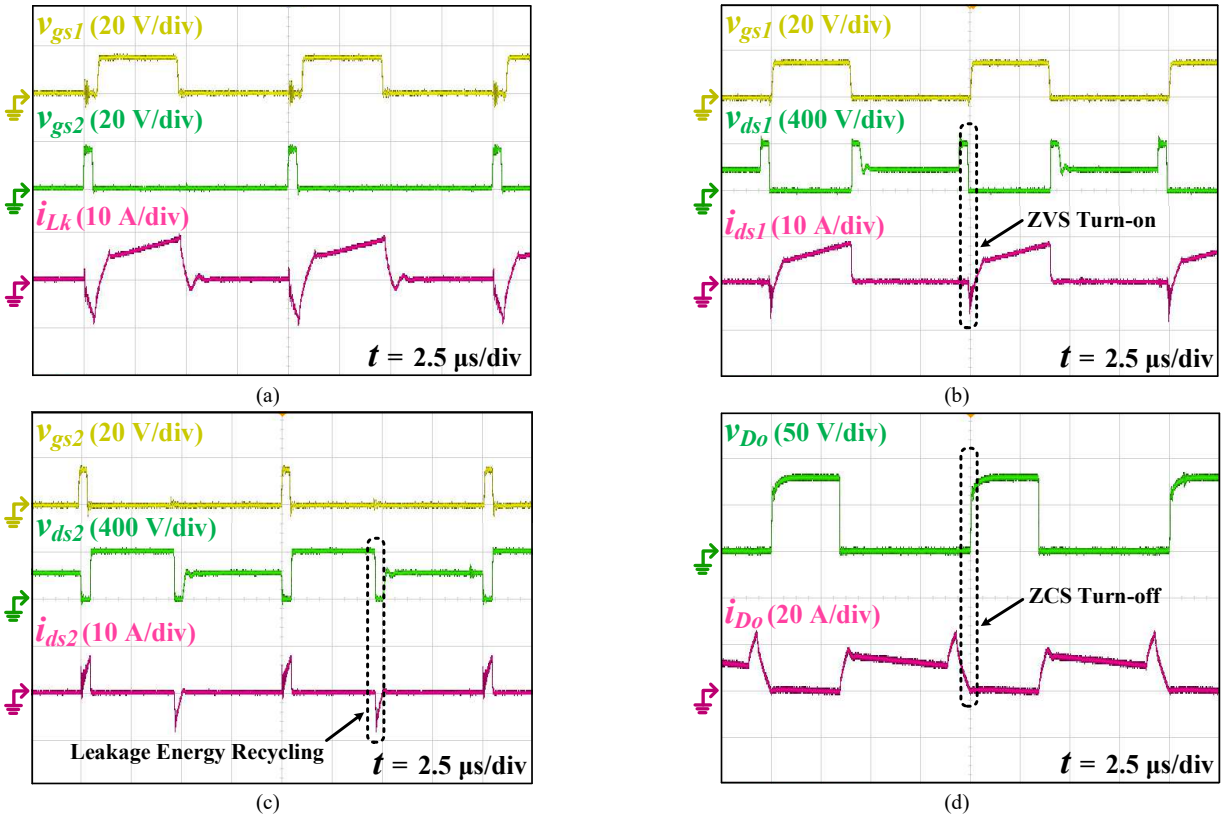


Fig. 14. Experimental waveforms of the prototype at full load. (a) Gate signals v_{gs1} and v_{gs2} and inductor current i_{Lk}. (b) Gate signal, voltage, and current of S_1. (c) Gate signal, voltage, and current of S_2. (d) Voltage and current of the diode D_o.

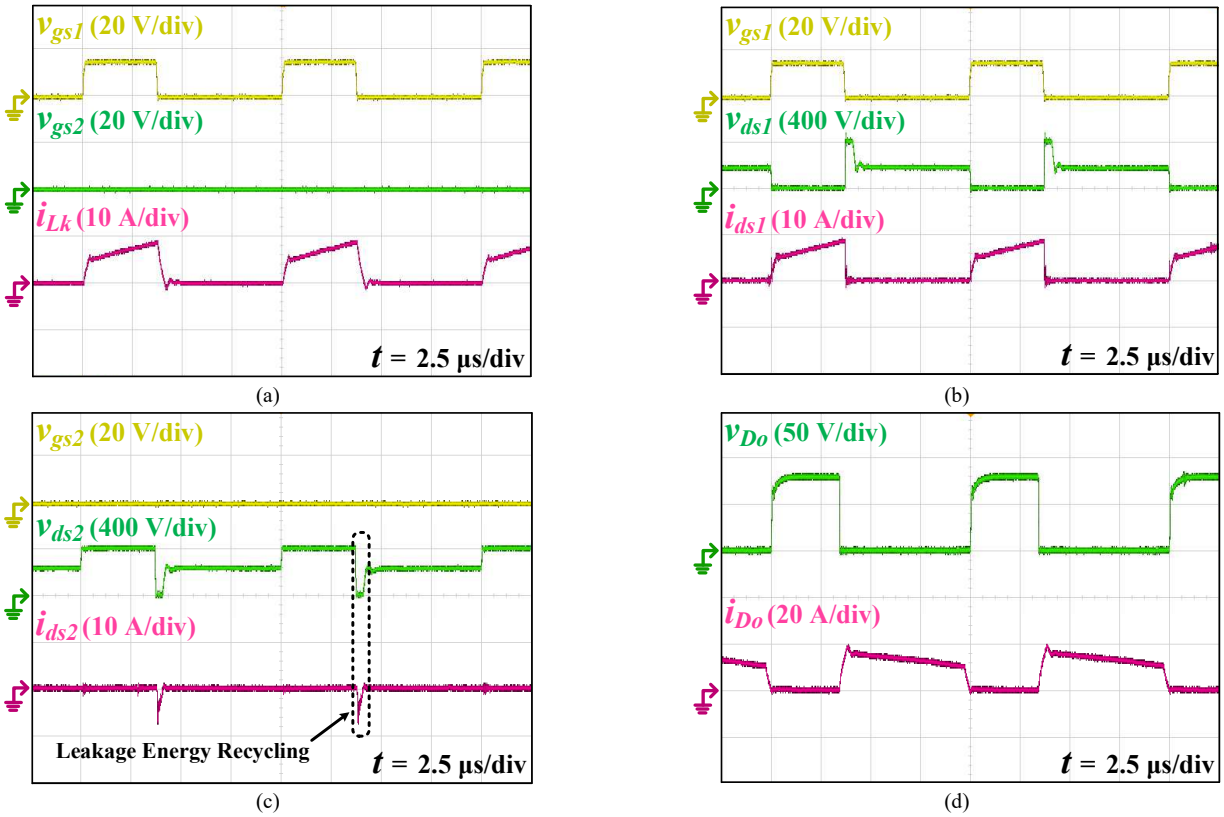


Fig. 15. Experimental waveforms of the prototype at full load under diode-only operation of S_2. (a) Gate signals v_{gs1} and v_{gs2} and inductor current i_{Lk}. (b) Gate signal, voltage, and current of S_1. (c) Gate signal, voltage, and current of S_2. (d) Voltage and current of diode D_o.

Fig. 16 shows the transient responses when the load of the 24 V HBAFC module changes between 20 and 200 W, with settling times of 2.75 and 2.5 ms for the load increase and decrease, respectively. When i_{o2} varies during the load transients, V_{o1} and V_{o3} remain constant, confirming the independent operation of the three HBAFC modules. Fig. 17 shows the measured responses when V_B is varied from 120 to 150 V with a ramp profile. The results show that the output voltages V_{o1}, V_{o2}, and V_{o3} of the three modules remain stable, verifying output-voltage regulation over the designed operating range and the dynamic response of the controller.

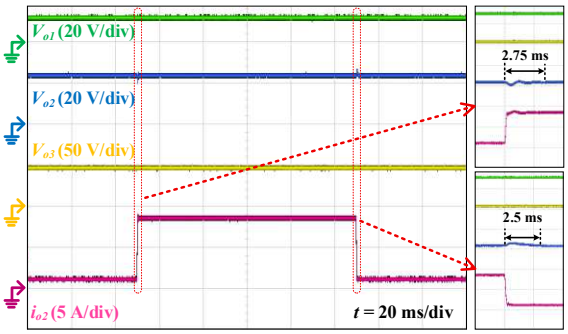


Fig. 16. Transient responses of the proposed HBAFC to load steps from 10% to 100% and from 100% to 10% of the rated load.

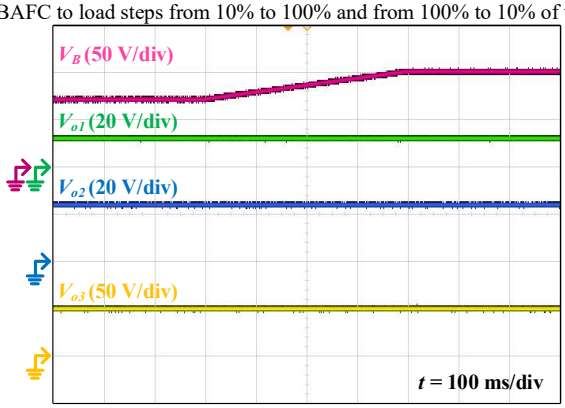


Fig. 17. Measured dynamic response of HBAFC under a linearly ramped battery voltage from 120 V to 150 V.

Fig. 18 shows the measured efficiencies of the 12-, 24-, and 48-V HBAFC modules at V_B = 120 V under active-switching and diode-only operation of S_2. Under active-switching operation of S_2, the full-load efficiencies of the 12-, 24-, and 48-V modules are 89.6%, 94.2%, and 96.1%, respectively. Under diode-only operation, the corresponding efficiencies are 87.2%, 92.6%, and 95.3%, respectively. In the active-switching mode, the reverse current introduces additional losses at light load, resulting in lower efficiency. As the load increases, the reduction in S_1 switching loss due to ZVS becomes more significant, resulting in higher efficiency at heavy loads. Fig. 19 shows the estimated loss distribution at full load. Owing to the inherent operating characteristics of the flyback converter, the output diode accounts for a considerable portion of the total loss.

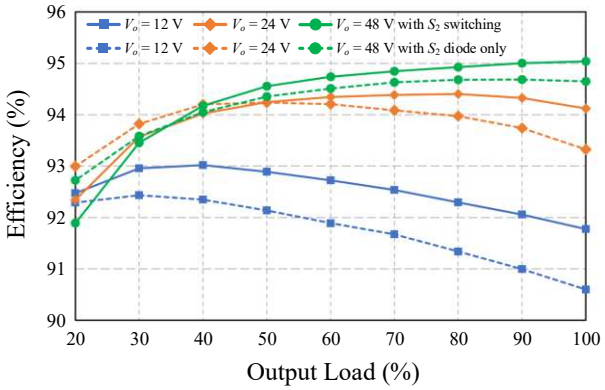


Fig. 18. Experimental efficiency of HBAFC.

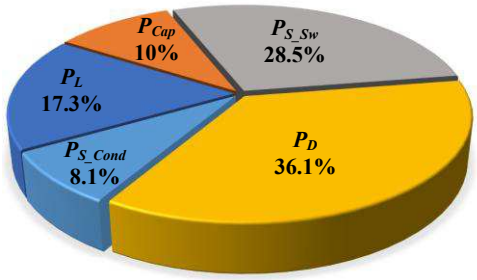


Fig. 19. Power loss distribution of HBAFC at full load.

VI. Conclusion

In this paper, the proposed HBAFC was experimentally validated in a common-ground HVDC bus-and-battery system using three 200-W modules with 12-, 24-, and 48-V outputs. The measured results confirmed that the modules operated independently without affecting other converters in the system and maintained regulated output voltages during load transients and as V_B varied from 120 to 150 V. With S_2 operated only as a diode, the HBAFC recycled leakage energy to the HVDC bus, clamped the main-switch voltage, and suppressed voltage and current ringing. The full-load efficiencies of the 12-, 24-, and 48-V modules under diode-only operation were 87.2%, 92.6%, and 95.3%, respectively. When S_2 was actively controlled, the reverse current in L_k enabled ZVS turn-on of the main switch, increasing the corresponding full-load efficiencies to 89.6%, 94.2%, and 96.1%, respectively. The output rectifier diode nevertheless remained the primary efficiency limitation. At the same power rating, a lower output voltage requires a higher output current, which increases diode conduction loss and reduces full-load efficiency. These results demonstrate that the proposed HBAFC provides a low-cost, independently regulated, and high-efficiency isolated power-conversion solution with reduced switching ringing, making it particularly suitable for industrial DC microgrids, factory DC distribution systems, and battery energy-storage systems.

Funding: The author received No Funding for this work.

Data availability statement: The data supporting the findings of this study are available from the corresponding author upon reasonable request.

Author contributions: C.-L. Shen supervised the project and provided research direction and theoretical guidance. H.-T. Huang conceived the proposed circuit topology and drafted the manuscript. Y.-L. Jian and C.-H. Shih performed the theoretical analysis, developed the hardware prototype, and collected and processed the experimental data. All authors reviewed and approved the final manuscript.

Conflict of interest: The authors declare no conflict of interest.

Additional information: The authors declare no competing interests. All authors confirm that no financial or non-financial relationships exist that could be perceived as influencing the results or interpretation of this study.

REFERENCES

1. Su, X. *et al.* Dynamic-loss-free stability enhancement for DC data center power systems with impedance-reshaped flying capacitor. *IEEE Trans. Power Electron.* **41**(8)**,** 13330–13343. https://doi.org/10.1109/tpel.2026.3668349 (2026).
2. Khan, I., Rahman, S., Ayaz, M. A., Amir, M. & Shehada, H. Review of isolated DC-DC converters for application in data center power delivery. *IEEE Trans. Ind. Appl.* **60**(4)**,** 5436–5446. https://doi.org/10.1109/tia.2024.3379305 (2024).
3. Wang, C., Zheng, P. & Bauman, J. A review of electric vehicle auxiliary power modules: challenges, topologies, and future trends. *IEEE Trans. Power Electron.* **38**(9)**,** 11233–11244. https://doi.org/10.1109/tpel.2023.3288393 (2023).
4. Mishra, J. & Shankar, A. Optimizing wind-PV-battery microgrids for sustainable and resilient residential communities. *Sci. Rep.* **15**(1)**,** 24339. https://doi.org/10.1038/s41598-025-06354-6 (2025).
5. Lee, G., Choi, S., Park, S., Hong, J. & Won, J. Development of an energy router for DC nanogrid-based building applications. *Sci. Rep.* **16**(1)**,** 23285. https://doi.org/10.1038/s41598-026-54044-8 (2026).
6. Chen, H., Lin, W.-m., Liu, W.-r. & He, W. Tapped-inductor bi-directional Cuk converter with high step-up/down conversion ratio and its optimum design. *Sci. Rep.* **12**(1)**,** 13745. https://doi.org/10.1038/s41598-022-17801-z (2022).
7. Vračar, D. Đ. Quasi-resonant flyback converter in an 800 V inductive charging system: abnormal operation and control aspects. *IEEE Access* **12,** 10804–10817. https://doi.org/10.1109/access.2024.3355013 (2024).
8. Ahmadi, S. M., Abjadi, N. R., Mirmoghtadaei, S. V. & Adib, E. A new forward-flyback converter without right half plane zero. *IET Power Electron.* **17**(15)**,** 2428–2438. https://doi.org/10.1049/pel2.12790 (2024).
9. Philipps, D. A., Blinov, A. & Peftitsis, D. On dead-time optimization and active gate driving in flyback converters with synchronous rectifiers. *IEEE Access* **12,** 173146–173155. https://doi.org/10.1109/access.2024.3462956 (2024).
10. Cruz-Cozar, J., Medina-Garcia, A., Morales, D. P. & Rodriguez, N. Resonant hybrid flyback: a novel topology with wide voltage range for DC microgrid applications. *Energy Rep.* **9,** 3222–3234. https://doi.org/10.1016/j.egyr.2023.02.027 (2023).
11. G., S. & N., A. P. An improved bi-switch flyback converter with loss analysis for active cell balancing of the lithium-ion battery string. *J. Electr. Comput. Eng.* **2024**(1)**,** 5556491. https://doi.org/10.1155/2024/5556491 (2024).
12. Zhao, Y., Chen, S. & Tang, Y. Research on high power density flyback converter with a new passive lossless snubber. *Int. J. Circuit Theory Appl.* **53**(8)**,** 4673–4681. https://doi.org/10.1002/cta.4326 (2025).
13. Pal, B. & Saha, S. S. A passive snubber for recovering leakage energy to output in a soft-switching flyback converter. *Electr. Eng.* **108**(3)**,** 190. https://doi.org/10.1007/s00202-026-03528-x (2026).
14. Tran, T. N. T., Li, H.-J., Chiu, H.-J. & Wang, J.-M. Triple-mode control scheme for an active-clamp flyback converter to improve efficiency at light-to-ultralight loads. *IEEE J. Emerg. Sel. Top. Power Electron.* **13**(5)**,** 5617–5631. https://doi.org/10.1109/jestpe.2025.3585286 (2025).
15. Tran, T. N. T., Xu, H.-Y. & Wang, J.-M. Development of active-clamp flyback converter for improving light-load efficiency. *IEEE J. Emerg. Sel. Top. Power Electron.* **12**(3)**,** 2456–2469. https://doi.org/10.1109/jestpe.2024.3387549 (2024).
16. Aydin, O. S. *et al.* Meta-heuristics based design and optimization of active clamp flyback converter for USB PD. *IEEE Access* **12,** 29269–29280. https://doi.org/10.1109/access.2024.3368861 (2024).
17. Yang, Y., Xi, J. & He, L. A highly integrated controller for active clamp flyback converter with optimized valley current and adaptive dead time control. *Microelectron. J.* **172,** 107134. https://doi.org/10.1016/j.mejo.2026.107134 (2026).
18. Cruz-Cozar, J. *et al.* Novel resonant bidirectional DC–DC converter based on asymmetrical half-bridge flyback. *IEEE Trans. Ind. Electron.* **73**(8)**,** 11612–11624. https://doi.org/10.1109/tie.2026.3666075 (2026).
19. Ding, S. *et al.* High-frequency high-power density multicell transformer-coupled input-series-output-parallel (ISOP) double clamp ZVS flyback converter. *IEEE J. Emerg. Sel. Top. Ind. Electron.* **6**(1)**,** 259–270. https://doi.org/10.1109/jestie.2024.3447776 (2025).
20. Saha, S. S., Konar, S., Pal, A. & Giri, A. A soft-switched flyback converter with leakage recovery snubber for class 2 LED driver. *Optik* **288,** 171209. https://doi.org/10.1016/j.ijleo.2023.171209 (2023).
21. Chakraborty, S. S., Dey, S. & Hatua, K. Design of a three-winding transformer for power decoupling of a three-port series resonant converter for an integrated on-board EV charger. *IEEE Trans. Power Electron.* **38**(11)**,** 14262–14273. https://doi.org/10.1109/tpel.2023.3308776 (2023).
22. Xu, J., Guo, J., Zhang, L., Xu, G. & Su, M. PWM controlled single stage resonant converter with multiwinding coupled inductor. *IEEE Trans. Power Electron.* **40**(11)**,** 16651–16663. https://doi.org/10.1109/tpel.2025.3586717 (2025).
23. Kieu, H.-P., Do, N.-Q. & Choi, S. Dual floating based three port DC-DC converter for EV-APM. *IEEE Trans. Power Electron.* **40**(3)**,** 4268–4278. https://doi.org/10.1109/tpel.2024.3508085 (2025).
24. Kozielski, K., Mudiyanselage, G. A., Narimani, M. & Emadi, A. A review of three-port integrated on-board charger and auxiliary power module in electric medium- and heavy-duty vehicles. *IEEE Open J. Power Electron.* **6,** 1347–1370. https://doi.org/10.1109/ojpel.2025.3587080 (2025).

25. Ibrahim, A. A. *et al.* EMI-silent operation of triple active bridge converters with online model-free ZVS optimization and RMS current reduction. *IEEE Open J. Ind. Appl.* **6,** 249–261. https://doi.org/10.1109/ojia.2025.3565905 (2025).
26. Huynh, K. K. N., Liang, T.-J., Tran, T. A. A. & Chen, K.-H. Three-port converter with leakage inductance energy recycling for high step-down applications. *IEEE J. Emerg. Sel. Top. Power Electron.* **11**(4)**,** 4453–4462. https://doi.org/10.1109/jestpe.2023.3265996 (2023).
27. Yu, G., Yadav, S., Dong, J. & Bauer, P. Revisiting the reverse switched current of buck, boost, and buck–boost converters in voltage-mode TCM–ZVS control considering parasitic resistances. *IEEE Trans. Power Electron.* **39**(7)**,** 8254–8268. https://doi.org/10.1109/tpel.2024.3382051 (2024).
28. Vazquez, A., Martin, K., Arias, M. & Sebastian, J. Variable-width hysteretic analog control for QSW-ZVS and TCM source/sink converters. *IEEE Trans. Power Electron.* **35**(3)**,** 3195–3207. https://doi.org/10.1109/tpel.2019.2929985 (2020).